Numerical Simulation of the Flow in the ONERA F1 Wind Tunnel

Sylvain Mouton
ONERA – Wind Tunnel Division, RD 53, 31410 Mauzac
FRANCE

sylvain.mouton@onera.fr

ABSTRACT

This paper presents the outcome of numerical simulations of the flow field inside the ONERA F1 wind-tunnel, which is a large-scale pressurized low-speed wind tunnel mostly used to investigate the take-off and landing performance of aircrafts in high-lift configuration. The simulations were carried out under RANS modelling assumptions. Results were compared to available experimental data characterizing the tunnel flow-field, especially in the test section. The overall flow physics is well captured by the simulations. However, when looking at the result with a more demanding level of accuracy, some important characteristics of the velocity distribution in the test section, such as flow upwash and total pressure distribution, are not replicated. Reasons are discussed in the paper, and some recommendations are derived for future similar simulations.

NOMENCLATURE

Symbols & definitions

A	=	local tunnel cross section
CAD	=	Computer Aided Design
CRM	=	Common Reference Model, see [1]
F1	=	large pressurized subsonic wind-tunnel located in Le Fauga-Mauzac test center, near Toulouse, France (F stands for **F**auga)
γ	=	ratio of specific heats for air, $\gamma = 1.40$
λ	=	pressure loss coefficient of the simulated leg of the tunnel
L_{ref}	=	reference length of the tunnel (1/10th of the square root of its cross-section, i.e. L_{ref} = 0.3967 m)
LRM	=	Large Reference Model: reference full-span model of the F1 wind tunnel, based on CRM shape
K	=	resistance coefficient through a porous obstacle, as in [2]
M	=	Mach number
p	=	pressure
q	=	dynamic pressure
Q	=	mass flow
Re	=	Reynolds number, based on the tunnel reference length L_{ref}
$\Sigma(M)$	=	ratio between the current cross section and the sonic cross section in a one-dimensional isentropic perfect gas
X, Y, Z	=	space coordinates from the center of the test section, X horizontal and streamwise, Y towards starboard, Z upwards
model volume	=	the volume in the test section where the model is intended to be positioned

Indices

0	=	index for the flow conditions averaged across model volume
1	=	index for the flow conditions at test section center ($X = Y = Z = 0$)
2	=	index for the flow conditions at the outflow plane of the simulation
ref	=	refers to one of the tunnel reference measurements

i   =   index for stagnation conditions
is   =   index for isentropic evolution

1   INTRODUCTION

In the past decades, simulation tools have matured enough to attempt modelling the flow in wind tunnels, which have been a primary source of aerodynamic data for more than a century. Simulating the flow in a wind tunnel, either empty or containing a model under test, can be attempted with different goals in mind, including at least:

- to fully replicate the aerodynamic setup while performing a "CFD validation experiment" [3];
- to improve the wall and support corrections that are applied to the results in order to extrapolate them to free-flow (e.g. [4]);
- to document the wind tunnel flow quality, aid the design of new wind tunnel parts, or the improvement of existing ones (e.g. [5]).

Many computational models of wind tunnels have been used in the past, most notably for wall correction activities [6]. The rise in computational power made RANS simulations more affordable and prompted their use to simulate wind tunnel flow, especially when previous modelling was known to show some weaknesses, e.g. in slotted [4][7] or porous [8] walls tunnels. The investigation reported in this paper was conducted in 2012, after similar activities from the same author and his colleagues [9]. At that time, the goals were to:

- assess the capability of RANS simulation to reproduce the mean flow field in the F1 empty wind tunnel;
- scrutinize the quality of this flow field in order to complement existing experimental data;
- prepare a computational model of the wind tunnel for possible subsequent use.

Therefore, this effort had no single application in mind, among the ones presented above. On the contrary, it was thought its outcome might be useful to different purposes, from wall corrections, or support corrections as in [10], to tunnel improvement.

2   GENERAL DESCRIPTION OF THE F1 WIND-TUNNEL

Only a brief description of the ONERA F1 wind-tunnel is given here to provide some context of the simulations carried out. The reader is referred to references [11], [12] and [15] for a more complete description. A photograph is shown in Figure 1, and a sketch in Figure 3.

Figure 1. General view of the F1 wind tunnel

The wind tunnel is of pressurized, closed-circuit type. The rectangular circuit is built of pre-stressed concrete and has an overall volume of some 13 000 m3. The settling chamber is 12 m in diameter and is fitted with a honeycomb filter (depth 200 mm, with 25 mm wide hexagonal cells) and three turbulence screens (5×5 mm cells, with wire of 1 mm diameter). It is followed by a metallic convergent which ensures the passage to the rectangular test section, with a 7.2 contraction ratio. The test section is 4.5 m wide, 3.5 m high and 11 m long. The first diffuser features a metallic part which ensures the gradual return to a circular cross section, with a mean aperture angle of 5°. The second part is a trunk of cone made of concrete, again with a total aperture angle of 5°. The first corner is 6.8 m in diameter. The wind-tunnel motor is a 9.5 MW asynchronous electric motor, driving a fan of 7.4 m diameter at a constant speed (360 RPM). The pitch angle of the 16 blades of the fan is controlled to adjust the tunnel speed.

To ensure a high productivity, the test section can be isolated from the rest of the circuit by two cylindrical sliding doors, which enables access to the model within 10 min maximum while keeping the rest of the circuit pressurized. The test section itself is mounted on a cart that can be removed from the aerodynamic circuit to carry the model and all the testing apparatus from and to different preparation cells in order to optimize the run-up time of the tunnel. A system of inflatable sealing is used to keep the different parts airtight. Some details will be further discussed when needed in section 6.1.

3   EXPERIMENTAL CHARACTERIZATION OF THE TUNNEL FLOW

This section explains how the experimental "empty tunnel conditions", or "uncorrected model conditions", (indexed "0") are related to the reference measurements (indexed "ref") produced by the facility instrumentation. This procedure has been in place for decades and follows the principles reminded in the more recently published reference [13].

In F1, reference flow conditions are obtained from the following reference measurements:
- total pressure $p_{i,ref}$ is obtained from a Pitot tube to the left hand side of the test section;
- static pressure p_{ref} is obtained from a reference static tap near the end of the convergent;
- total temperature $T_{i,ref}$ is measured from a thermocouple (type T) in the settling chamber.

The characterization of the flow in the test section consists in:
- *tunnel calibration*: establish relationship between the state of the flow in the model volume, and the reference measurements;
- *flow quality*: measure the homogeneity of the flow (spatial uniformity) in the model volume and its turbulent content (temporal uniformity).

3.1   Total temperature calibration

Measurements of total temperature were carried out during the tunnel commissioning test in 1976. The total temperature $T_{i,0}$ was found equal to $T_{i,ref}$ and homogeneous across the test section within ±0.5°C [14].

3.2   Total pressure calibration

The total pressure distribution in the test section was measured using rakes of Pitot probes mounted and displaced in between the tunnel walls. A small deficit of total pressure exists in the test section compared to the total pressure at the periphery of the stream, where reference total pressure taps are located. Examined in areas where full-span models are located, the average value of the total pressure coefficient is:

$$K_{pi,cal} = \frac{p_{i,ref} - p_{i0}}{q_{ref}} = 0.005$$

This value of $K_{pi,cal}$ was found to be independent of Mach and Reynolds numbers and forms the tunnel calibration law for the total pressure.

In terms of homogeneity, deviations of $K_{pi} = \frac{p_i - p_{i0}}{q_0}$ across the span of the model are within ±0.003. The static pressure being uniform there, this means that the velocity in model volume is homogeneous within ±0.15% of its average value. Some plots will be provided in section 5.5, when comparing simulation with

3.3 Static pressure calibration

The static pressure along the tunnel centreline is measured using a long pipe, as in many other tunnels [13]. Thank to proper side wall divergence, the static pressure is homogeneous within $\pm0.2\% \times q_0$ in the model volume. Again, a plot will be provided latter, in section 5.3, with comparisons to simulation data.

The difference in static pressure between the tunnel centreline and the static reference tap forms the tunnel calibration law for static pressure:

$$K_{p,cal} = \frac{p_{ref} - p_0}{q_{ref}} = K_{p,cal}(M_{ref}, Re_{ref})$$

A polynomial regression of $K_{p,cal}$ is performed against M_{ref} and Re_{ref} to come up with an analytical law $K_{p,cal}(M_{ref}, Re_{ref})$ that is used during tunnel run to determine the static pressure, and therefore the Mach number, as detailed in section 3.5. Actually, each of the redundant reference taps has its own calibration law.

3.4 Flow upwash and sidewash angles

In F1, the most accurate measurement of average upwash angle is obtained with model inversion method [16]. It provides a value representing the upwash angle averaged along a full model span. A value of +0.11°±0.02° was recently measured with the standard LRM model (based on CRM shape), without tail plane (unpublished results). Previous measurements with another tailed model resulted in a value of +0.16°±0.03° reported in [17]. The 0.05° difference was due to measurement uncertainty and an increase of upwash (at tail location only) because of the imperfect symmetry of the support.

Tests reported in [17] using a special setup for high-accuracy PIV measurements gave access to the spatial distribution of flow upwash angle with an unprecedented level of detail, and an accuracy level estimated at ±0.05°. It was found that the spread around mean upwash was within ±0.15° over the span of a typical 3 m full span model, see Figure 2. This had already been observed previously with 5-hole probes, but with a lower accuracy and much sparser measurements. New improved PIV measurements (unpublished results) confirmed these results, and further refined the knowledge of the flow across the span of the model. Once averaged across a standard model span of 3 m, the PIV measurements yielded an average upwash angle of +0.09°±0.03°, therefore providing confirmation of the traditional model inversion method. Sidewash angle were also measured and were found to be near zero, but with an accuracy level of only about ±0.15° (because measuring the sideslip angle was not an objective of the test).
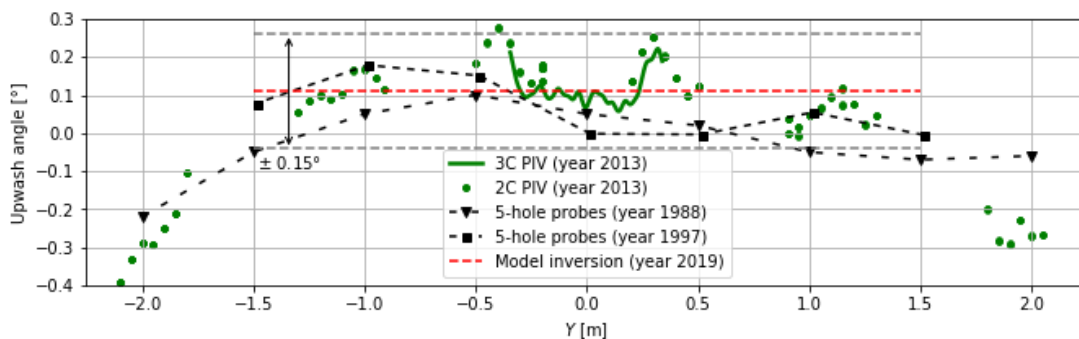

Figure 2. Spanwise distribution of upwash angle in the middle of the test section (from [17])

3.5 Use of tunnel calibration during test

The total temperature at tunnel center is considered equal to the settling chamber reference temperature $T_{i,ref}$ (from results presented in section 3.1), hence: $T_{i0} = T_{i,ref}$.

Total and static pressures $p_{i,ref}$ and p_{ref} are combined to compute the reference Mach number M_{ref} and

dynamic pressure q_{ref}, using classical isentropic formulae:

$$M_{ref} = \sqrt{\frac{2}{\gamma-1}\left(\left(\frac{p_{i,ref}}{p_{ref}}\right)^{\frac{\gamma-1}{\gamma}} - 1\right)} \tag{1}$$

$$q_{ref} = \frac{\gamma}{2} p_{i,ref} M_{ref}^2 \left(1 + \frac{\gamma-1}{2} M_{ref}^2\right)^{-\frac{\gamma}{\gamma-1}} \tag{2}$$

With the help of the total pressure $T_{i,ref}$ and the tunnel standard reference length L_{ref}, the reference Reynolds number Re_{ref} is also computed.

It has to be clearly understood that these "ref" quantities characterize the flow field existing at the location of the reference taps, not at the location of the model. It would therefore make no sense to use these values in processing any model measurement (e.g. in calculating force coefficients).

Then, the average total pressure at model location p_{i0} is deduced from the tunnel reference measurement $p_{i,ref}$ to account for the total pressure deficit exposed in section 3.2:

$$p_{i0} = p_{i,ref} - K_{pi,cal}\, q_{ref} \tag{3}$$

In a similar way, the static pressure at model location is obtained from the tunnel calibration law exposed in section 3.3:

$$p_0 = p_{ref} - K_{p,cal}(M_{ref}, Re_{ref})\, q_{ref} \tag{4}$$

Once total and static pressure at model location are determined, isentropic formulae are again used to compute the Mach number at model location:

$$M_0 = \sqrt{\frac{2}{\gamma-1}\left(\left(\frac{p_{i0}}{p_0}\right)^{\frac{\gamma-1}{\gamma}} - 1\right)} \tag{5}$$

Every other quantity at model location can be deduced using classical isentropic relationships. These quantities are called the "empty tunnel conditions", or "uncorrected model conditions" (uncorrected from wall and support interference). This is the flow as it exists in the model volume before actually putting the model in the tunnel. Interestingly, the flow temperature plays almost no role in determining the Mach number and dynamic pressure, and therefore accuracy requirement on temperature measurement is less stringent than on pressure measurements.

Every reference measurement is made redundant, with at least two independent sensors. For the most critical parameter, namely the differential pressure measurement between p_{ref} and $p_{i,ref}$, no less than 6 static pressure taps, independently connected to 3 total pressure taps, using 6 different sensors of 3 different types, are used. Agreement between redundant measurements is automatically checked during each tunnel run.

Mean upwash and sidewash angles are accounted for when computing uncorrected aerodynamic angles (angle of attack and sideslip angle, once again, uncorrected from wall and support interference) from geometric angles (pitch, yaw and azimuth angles).

3.6   Comments

The flow homogeneity at the location of a typical full-span model compares favourably with requirements from two different literature sources, see Table 1. More detailed data will be presented in the following sections when comparing simulations and experimental results.

Table 1. Recommended flow uniformity across model volume

	Dynamic pressure	Flow angle	Total temperature
AGARD AR-184 [18]	$\pm 0.5\% \times q_0$	$\pm 0.1°$	± 1 K
Low-Speed Wind Tunnel Testing ([16] section 6)	$\pm 0.5\% \times q_0$	$\pm 0.1°$ to $\pm 0.2°$	-
Achieved in F1	$\pm 0.3\% \times q_0$	$\pm 0.15°$	± 0.5 K

4 COMPUTATIONAL MODEL

4.1 Tunnel geometry

The simulations presented in this paper were carried out over a domain comprised between the settling chamber and the first corner downstream of the test section (see Figure 3). The walls were assigned a no-slip adiabatic boundary condition to generate boundary layers.
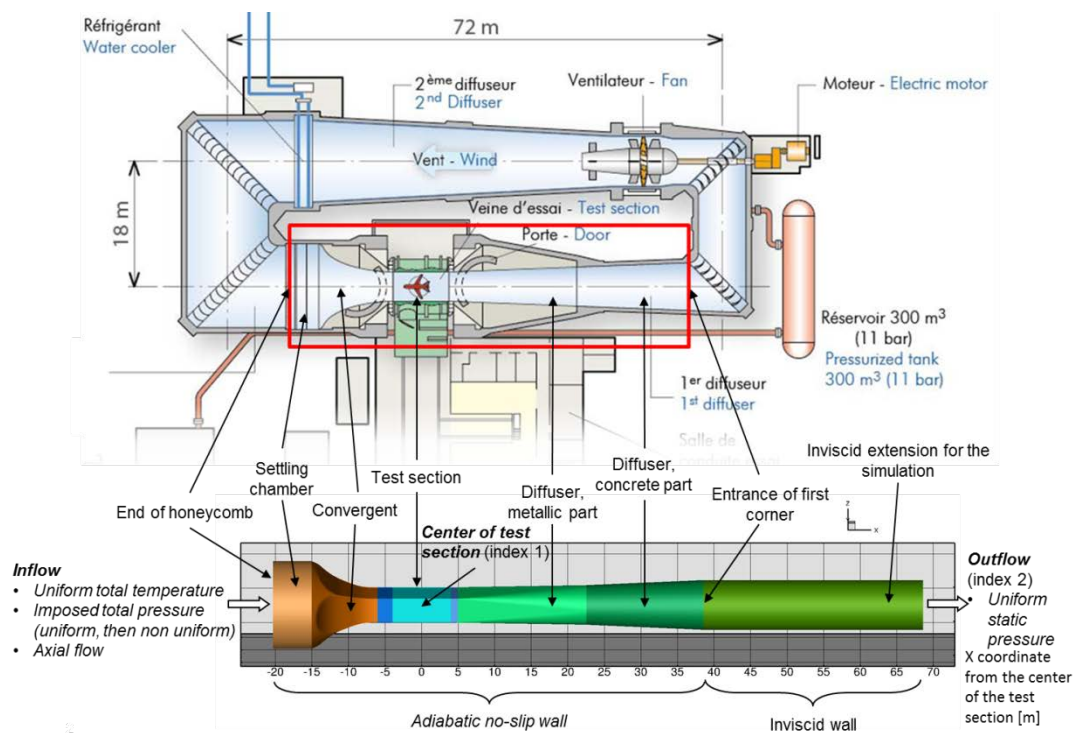

Figure 3. Overview of F1 wind tunnel and corresponding simulation domain with boundary conditions

The CAD shape of the wind tunnel was constructed from the original drawings, except for the side walls of the test section (-4 m $< X < +4$ m). These side walls are slightly diverging to compensate the growth of the boundary layers in the test section and therefore achieve a uniform velocity distribution along the centerline. The divergence of the tunnel side walls was adjusted to its today's position in 1988 and their final shape was measured at this time. These measurements were integrated in the CAD model. The floor and ceiling of the test section are flat and horizontal.

This physical domain was further extended 30 m downstream (4.4 local diameters) by a tube of constant cross-section with inviscid wall boundary condition. This was intended to resorb any flow separation that could occur in the diffuser. Indeed, in previous research [9][19], it was identified that flow separation could occur in the diffuser, at least during the convergence process, and that such reverse flow reaching the outlet surface would cause the solver to become unstable and then to crash.

Some features of the geometry were neglected in the simulations due to their geometrical complexity:

- the honeycomb and the three turbulence screens located in the settling chamber (to be discussed in section 6.1);

- the venting slot and porous part immediately in front of the start of the convergent (to be discussed in section 6.3);

- the venting slot at the downstream end of the test section.

4.2   Upstream and Downstream Boundary conditions

The inflow surface was given a subsonic injection boundary condition, i.e. the total temperature, total pressure and flow direction are imposed. For all computations, a uniform total temperature of 298 K was imposed and the injected flow was assumed aligned with the *X*-axis. Concerning the total pressure, it was also assumed uniform in the first place, with a value varying between 1 and 3.85 bars, representing the pressure operating range of the tunnel. In the second place, a slightly non-uniform distribution was imposed as will be presented in section 5.5.

The outflow surface was assigned a subsonic outflow boundary condition, for which the static pressure is imposed. One of the difficulties of simulating a wind tunnel flow is that one does not know in advance which value of the back pressure to use in order to generate the required Mach number in the test section. In these simulations, the back pressure value was iterated during the convergence process with the help of a proportional-derivative controller algorithm that will be now presented.

Let us index "1" the flow conditions at the center of the test section ($X = Y = Z = 0$) and "2" the flow conditions at the outflow, and call A the tunnel cross-section. Let us note $\Sigma(M)$ the ratio between the current cross section and the sonic cross section in a one-dimensional isentropic perfect gas:

$$\Sigma(M) = \frac{1}{M}\left(\frac{2}{\gamma - 1} + \frac{\gamma + 1}{\gamma - 1}M^2\right)^{\frac{\gamma+1}{2(\gamma-1)}} \tag{6}$$

We note $\Sigma'(M)$ the derivative of this function and $\Sigma^{-1}(M)$ its inverse over the subsonic interval $M < 1$. To simplify notations, we note $\tau(M)$ the function:

$$\tau(M) = 1 + \frac{\gamma - 1}{2}M^2 \tag{7}$$

Let us try to reach a tunnel Mach number M_1 in the center of the test section. If the flow was one-dimensional and isentropic in the tunnel, the Mach number at the outflow $M_{2,is}$ would be:

$$M_{2,is} = \Sigma^{-1}\left(\frac{A_2}{A_1}\Sigma(M_1)\right) \tag{8}$$

with $\frac{A_2}{A_1} = 2.31$ in our case. The outflow pressure would then be:

$$p_{2,is} = p_{i1}\ \tau(M_{2,is})^{-\frac{\gamma}{\gamma-1}} \tag{9}$$

The actual flow being not isentropic, the actual outflow pressure p_2 is smaller than $p_{2,is}$ because of the head loss associated with entropy generation in the boundary layers. We then define the pressure loss coefficient λ of the simulated tunnel as:

$$\lambda = \frac{p_{2,is} - p_2}{q_1} \tag{10}$$

The sensitivity of the outflow pressure with respect to the tunnel Mach number is therefore:

$$\frac{\partial p_2}{\partial M_1} = \frac{\partial p_{2,is}}{\partial M_1} - \frac{\partial \lambda}{\partial M_1} q_1 - \lambda \frac{\partial q_1}{\partial M_1} \tag{11}$$

where all partial derivatives are taken at constant total pressure. In the present work with subsonic Mach numbers, it was considered that $\frac{\partial \lambda}{\partial M_1} \ll 1$ and $\lambda \ll 1$, and consequently only the first term was retained. Then, taking into account the equation (9) for $p_{2,is}$ one can develop equation (11) into:

$$\frac{\partial p_2}{\partial M_1} \approx -p_{2,is} \frac{\gamma M_{2,is}}{\tau(M_{2,is})} \frac{A_2}{A_1} \frac{\Sigma'(M_1)}{\Sigma'(M_{2,is})} \tag{12}$$

A simple discrete-time proportional-derivative controller algorithm iterating on the back-pressure (sketched in Figure 4) was then implemented to converge the tunnel Mach number toward the target M_1 as quickly as possible. This algorithm examines the tunnel Mach number every $n_{control}$ iterations and outputs corrections to be applied the back pressure p_2. Iterations here are full multigrid cycles (see section 4).

The proportional coefficient of this algorithm is chosen to be $K = 0.7 \times \frac{\partial p_2}{\partial M_1}$, where $\frac{\parti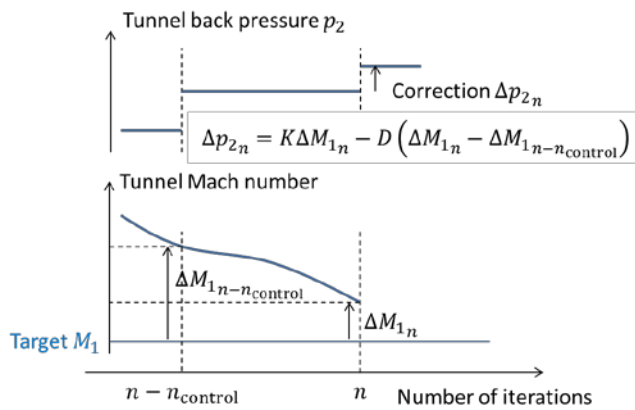al p_2}{\partial M_1}$ is given by Eq. (12) and 0.7 was chosen as a damping coefficient to keep the algorithm stable. The derivative coefficient was chosen as $D = K \frac{n_{charac}}{n_{control}}$ where n_{carac} is an approximate characteristic response time of the simulated tunnel, evaluated with the help of a preliminary calculation during which the tunnel is converged to an arbitrary Mach number and is then imposed a step change in back pressure. Numerical values were selected to be $n_{control} = 200$ iterations, and $n_{carac} = 2000$ iterations. The first 1 500 iterations are carried out without changing the back pressure in order for the flow to settle before starting the control process.

Figure 4. Algorithm for back pressure control

For the first calculation with $M_1 = 0.20$, the back pressure is initialized using equation (10), with λ being given a first guess value of 0.067, estimated from textbook methods ([16] chapter 3). The flow is initialized as uniform with a Mach number equal to 0.05 everywhere. The simulation is allowed to run for 20 000 iterations, a number sufficient to converge both the computation and the tunnel Mach number as shown in Figure 5.

Some of the subsequent simulations were restarted from previously obtained flow-field, and the initial guess for λ was improved calculations after calculations, but the gain in the necessary number of iterations was small.

The control equations exposed above were written for the most general case where the flow at test section center (indexed 1) is different from the flow averaged across model volume (indexed 0). In F1 wind-tunnel, the static pressure is practically uniform in the test section so that $p_1 = p_0$. In the same way, in simulations with uniform total pressure, one has $p_{i1} = p_{i0}$. In simulations with non-uniform pressure, p_{i1} is lower than p_{i0} by about $0.1\% \times q_0$ (see Figure 15 in section 5.5), which is of little consequence.
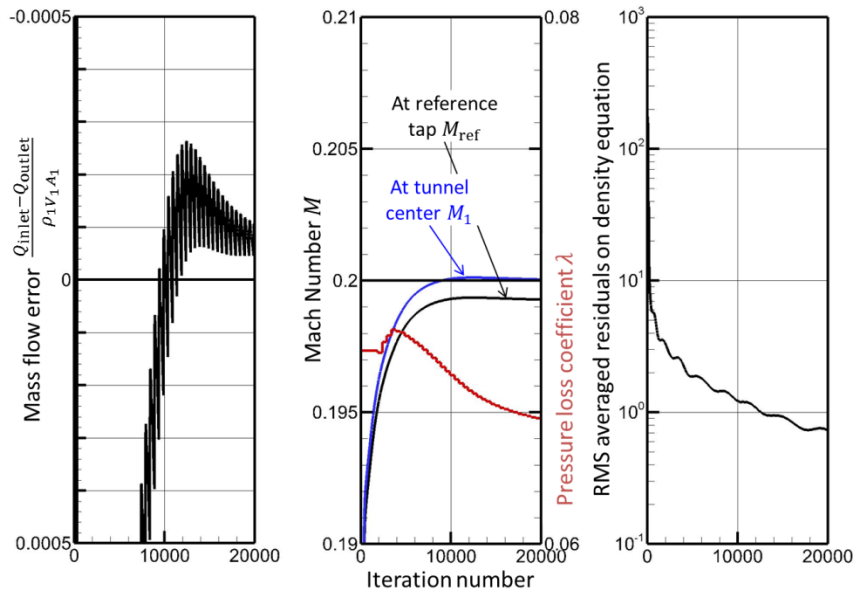
Figure 5. Convergence history of the simulation at p_{i0} = 2 bars, $M_0 = M_1$ = 0.2

Of course, in case a model and support are placed in the virtual tunnel, the pressure loss coefficient should be increased to account for the drag of these objects. In simulations with models carried out in [25][27], the back-pressure was also driven by an iterative process, but it was formulated as an optimization process (to "pair" the flow-field with the free-flow situation) rather than a dynamic control algorithm (to reach a predefined Mach number in the tunnel).

4.3 Tunnel mesh

The wind tunnel was discretized with a structured multiblock mesh comprising 2 321 900 cells. In the test section, the cells measured about 16 cm × 7.8 cm × 5.6 cm, respectively in *X*, *Y* and *Z* directions. The first cell near walls was about 3 μm thick, which allowed resolving the boundary layers with about 30 mesh cells, down to the viscous sublayer, with *y+* in the range 0.3–0.5 at the lowest Reynolds number, and 1–2 at the highest Reynolds number. A view of the resulting mesh is provided in Figure 6.
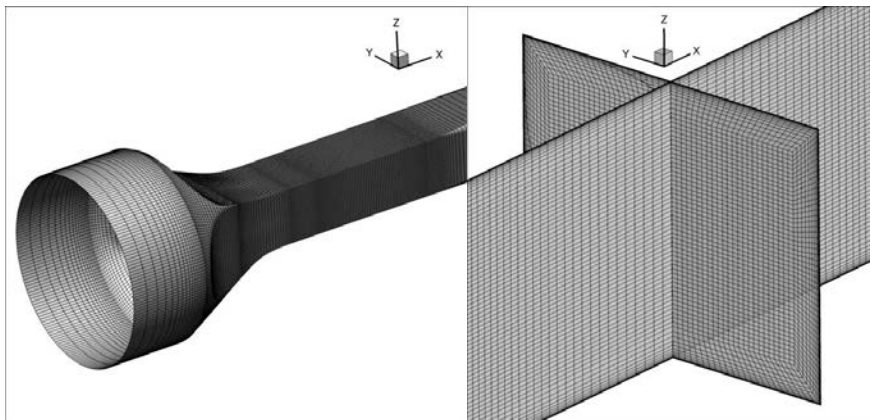

Figure 6. View of the computational structured multiblock mesh

4.4 Flow equations and resolution

The flow in the tunnel was modelled using RANS equations with the Spalart-Allmaras turbulence model. The *elsA* solver [20] version 3.4.03 was used. Space discretization used a finite-volume formulation with the

second order scheme of Jameson, with zero second order dissipation and a low fourth order scalar artificial dissipation coefficient of 0.016, completed by Martinelli correction with an exponent of 0.3. Time discretization scheme was first order, with an implicit formulation solved using a LU-SSOR method. Regarding the low Mach number implied, Choi-Merkle preconditioning was used in the calculation. Convergence was accelerated by the use of a 2-level multigrid method.

5   COMPARISON BETWEEN SIMULATED AND OBSERVED FLOW FIELD

Unless otherwise indicated, simulation results are presented for a tunnel total pressure p_{i0} of 2 bar and a Mach number M_0 of 0.20. If available, experimental data are selected at similar flow conditions. If not available, the nearest flow conditions are plotted and are indicated on the figures.

The simulations were carried out for 6 different flow conditions in the tunnel, indicated in Figure 7.
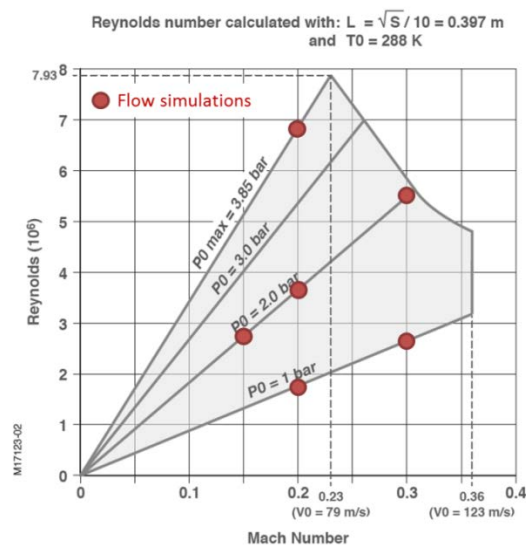

Figure 7. F1 wind tunnel operating range, with flow simulations performed

5.1   General flow features

The Figure 8 displays a general view of the obtained flow field. At first glance, a rather simple flow field is obtained, as one could expect: a mostly inviscid flow, almost incompressible, surrounded by boundary layers that are mostly 2D and subject to moderate pressure gradients.
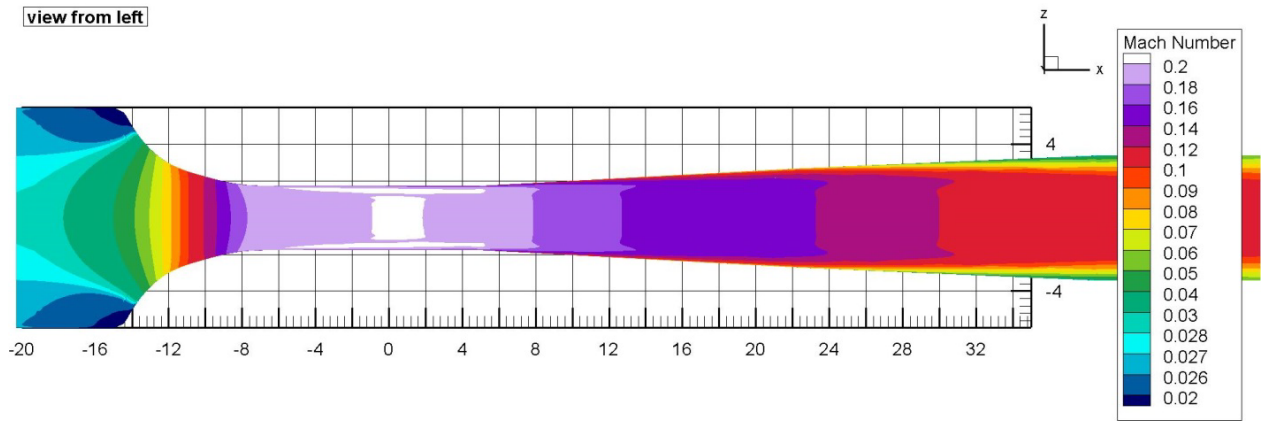
Figure 8. Overall simulated Mach number distribution in the wind tunnel

The overall correctness of the simulations is first validated by examining the distribution of static and total pressure along the circuit. Experimental measurements were carried out during tunnel commissioning in 1977 [14][15]. Some of these measurements used provisional pressure taps connected to water manometers over hundreds of meters of tubing. Although their reading was less reliable than today's usual pressure sensors, they give a good indication of the pressure recovery in the first part of the diffuser. The simulated flow field is in good agreement, see Figure 9. Profiles of total pressure at two stations in the diffuser are shown in Figure 10, with again a good agreement.
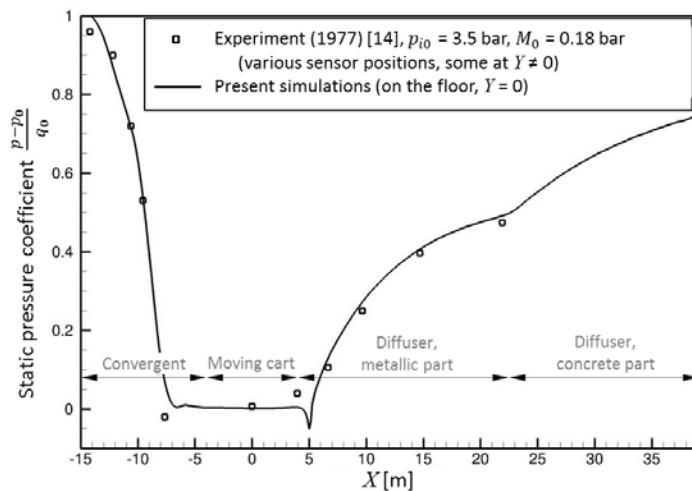

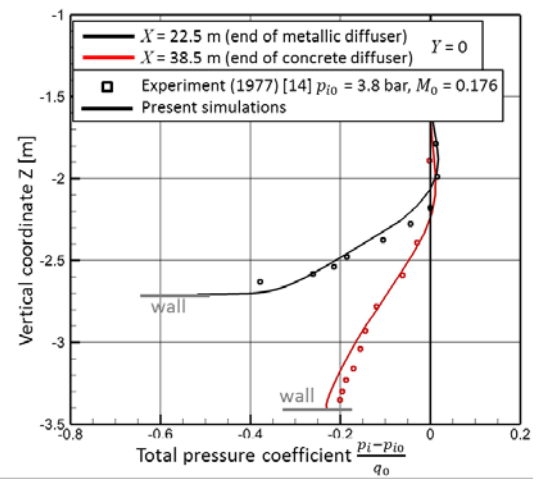**Figure 9. Distribution of static pressure along the tunnel leg**

Figure 10. Distribution of total pressure in the diffuser

5.2   Boundary layers in the test section

Next, the thickness and profile of the turbulent boundary layer is examined on the test section walls. Data from several rakes are available, and the agreement is generally fair. An example of boundary layer profile is shown near the entrance of the test section in Figure 11.
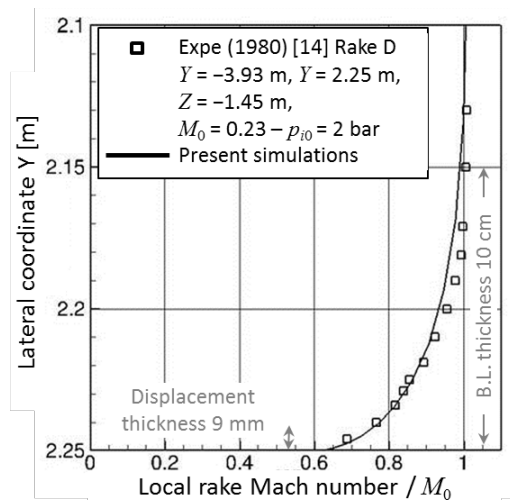
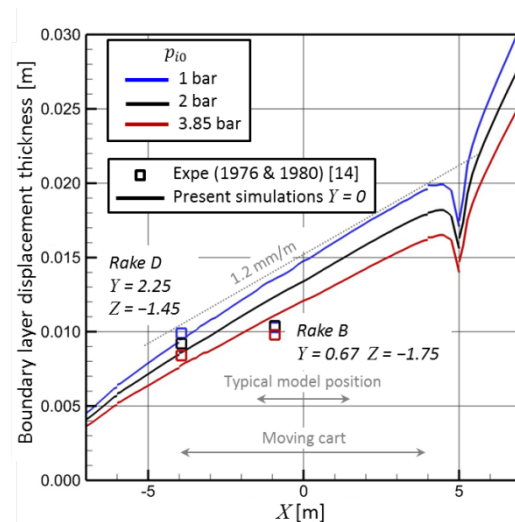**Figure 11. Boundary layer profile in the test section**

Figure 12. Boundary layer displacement thickness in the test section

The boundary layer displacement thickness grows in the test section, at a rate of about 1.2 mm/m. This rate of growth is larger at low Reynolds number, see Figure 12. In the simulations, at a given X coordinate, the predicted boundary layer thickness is identical on all test section walls, except near corners. This is not exactly the case experimentally (based on other probes, not shown in the figure). Also, the boundary layer downstream of $X = 0$ is not well documented, with measurements carried out with a single rake sparsely equipped in pressure taps (not shown).

5.3   Flow Uniformity along test section centreline

Experimentally, the uniformity of the velocity along the tunnel centreline is measured using the long static pipe that is also used to determine tunnel calibration, as in many other facilities [13]. A comparison in terms of pressure coefficient is provided in Figure 13. In simulations as well as in measurements, the flow velocity is uniform within ±0.1% over 5 m long. This is a result of careful adjustment of wall divergence. Simulations indicate that the very small velocity gradient existing at low Reynolds number ($p_{i0} = 1$ bar in Figure 13) is even reduced at higher Reynolds number ($p_{i0} = 3.85$ bar), due to the reduced rate of growth of boundary layers on the wall (as shown in Figure 12). This trend with Reynolds number possibly exists in the measurements but is obfuscated by the small scatter (about 1.5×10^{-3} rms) in experimental data.

This small scatter stems from sensor noise, but mostly from small flaws in the tap geometry, repeatable from one test to another. Therefore, the mean of about 30 taps located at typical full model position (-1.5 m $< X <$ 1.5 m) is used to estimate tunnel static pressure p_0.
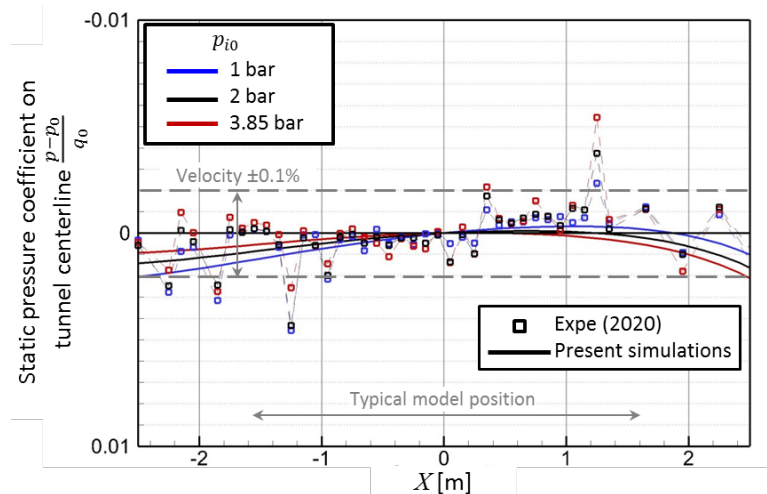
Figure 13. Distribution of static pressure on tunnel centreline

## 5.4   Flow Uniformity across the test section

Detailed results are presented in Figure 14, for a tunnel total pressure p_{i0} of 2 bar and a Mach number M_0 of 0.20. They are very similar for other flow conditions.

After simulations were carried out, examination of the CAD model revealed that there was a "dip" of 14 mm around X=−3 m on the starboard vertical wall. This spurious geometrical feature was caused by improper interpolation between wall position measurements during the setup of the CAD model. The real wall is flat within ±2 mm there. Since the error did not impact the flow in the model volume, it was not corrected.

Another non-physical feature that can be observed in a overshoot of total pressure by about 0.8% $\times q_0$ at the top of the boundary layer. This is an unexplained artefact of the simulation, probably related to an insufficient discretization of the transport equation for the turbulent viscosity at the top of the boundary layer. This is not uncommon (e.g. it was also observed in [21], fig. 6b, in similar simulations with FUN3D software) and it generally gets unnoticed unless an extreme scale-up is used (< 1% of outer velocity), as in the present paper.
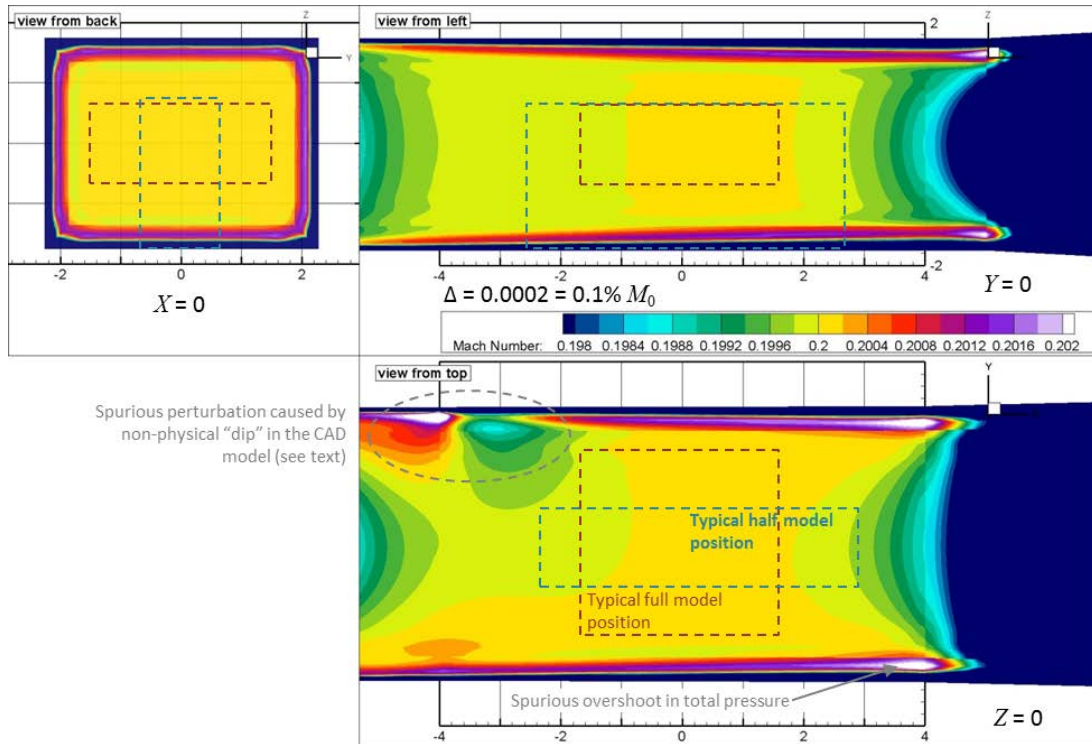
a. Mach number
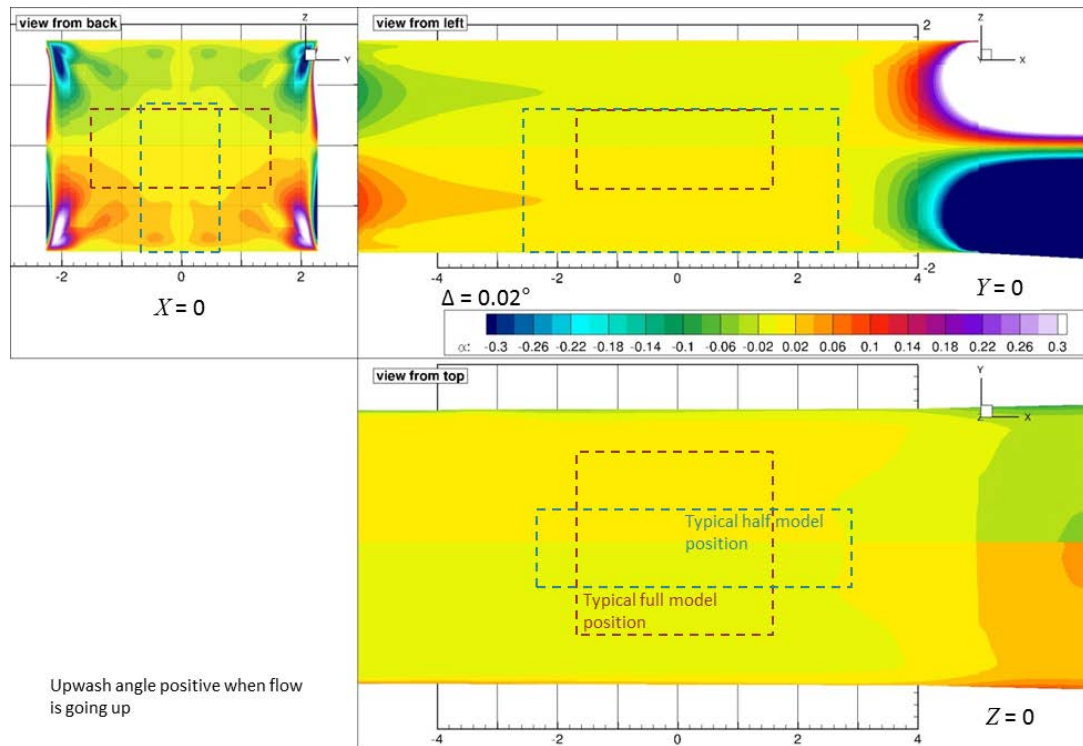
b. Upwash angle

Figure 14 (continued on next page). Simulated flow field the test section
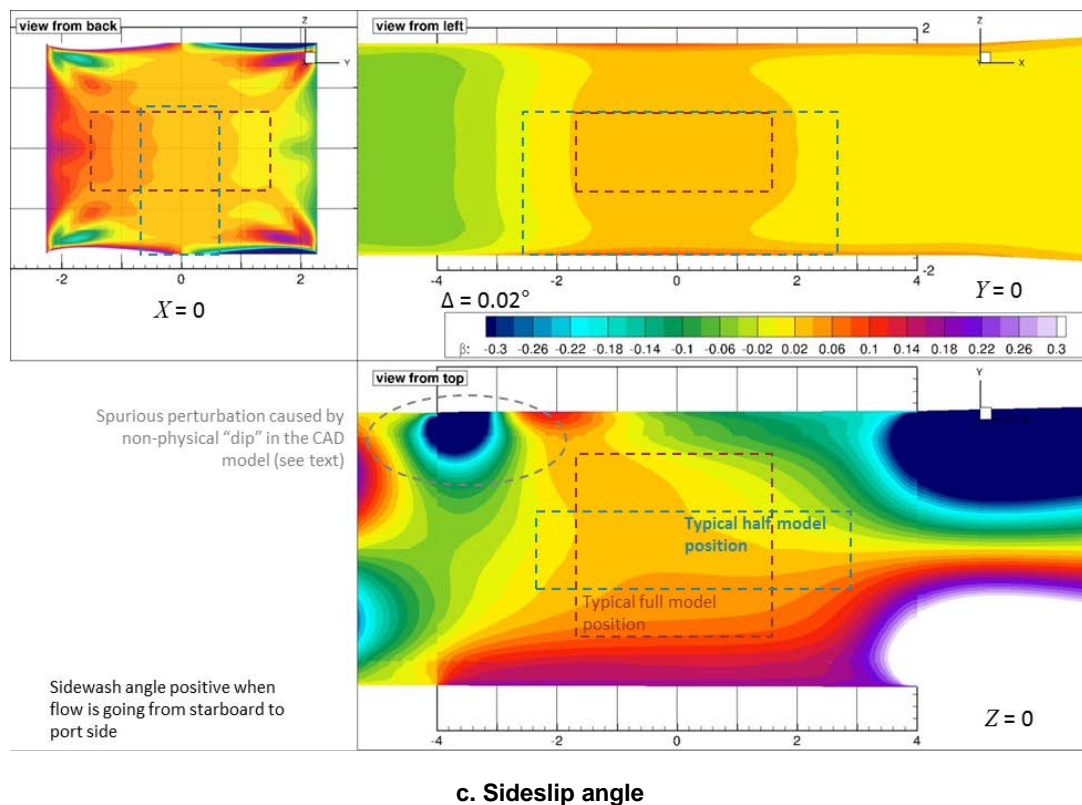
c. Sideslip angle

Figure 14 (concluded). Simulated flow field the test section

Apart from these well identified flaws in the calculations, and in spite of the extreme scale-up used in the figures (iso-lines every 0.1% in velocity and every 0.02° in angles), the simulated flow appears to be almost perfectly uniform and lined up with the X axis in the typical model volume.

To summarize the situation: having introduced a uniform flow at the inlet, we get a uniform flow in the test section. The tunnel geometry, as it is designed (e.g. wall divergence) and simulated, introduces no significant distortion in most of the test section, especially in the model volume.

Although the real tunnel flow is indeed nearly uniform, there are some features that are not reproduced by the simulations, namely the flow angle (see section 3.4), and the total pressure distribution across the test section, to be discussed in the next section.

5.5   Change in inlet boundary condition to reproduce total pressure distribution

In the early years of the tunnel, it was measured that the total pressure on the periphery of the test section is, on average, about 0.5% $\times$ q_0 higher than in the model volume. Since total pressure probes are located near the walls, this needs to be accounted for, as described in the total pressure calibration in section 3.2.

Since this small total pressure deficit is not picked up in the simulations presented so far, it was likely originating from the settling chamber. Therefore it was attempted to introduce a non-uniform total pressure distribution on the inlet boundary condition.

To explain the phenomenon, the following hypothesis was proposed. When approaching the entrance of the convergent, the flow velocity gets higher near the middle of the settling chamber (see Figure 8). It therefore crosses the turbulence screens with a higher dynamic pressure near the middle of the settling chamber, causing higher pressure loss than on the periphery.

The dynamic pressure was examined on the inlet plane of the previously obtained simulations, and it is

indeed about 12% to 18% higher near the tunnel centreline than on the periphery. It was then decided to make the inlet total pressure deficit proportional to this local inlet dynamic pressure. It was then calculated that a resistance coefficient K of 1.5 through the honeycomb and screens was requested to match the total pressure profile in the test section. The order of magnitude compares favourably with the resistance coefficient measured during tunnel commissioning in 1976, which varied from 1.6 to 2.6, but including also the 4th corner, upstream of the honeycomb [14].

The non-uniform total pressure distribution hence calculated was applied on the inlet and the calculations were run again. Examination of the flow field reveals that the profile of total pressure is simply convected without diffusion from the inlet to the test section. The distribution of total pressure in the test section finally obtained is depicted in Figure 15.

The shape and amplitude of the profile is well reproduced by the simulations, with the exception of the lower part of the test section ($Z < 0$), where the measurements are asymmetrical and an additional deficit of 0.1% to 0.2% $\times q_0$ exists. An explanation for this phenomenon may stem from the asymmetrical deformation of the screens under the combined wind and gravity loading. This hypothesis was examined in [17] and may indeed be a valuable explanation. Another possible explanation would be the tendency of the screens to accumulate dust in their lower part, which would locally increase the resistance coefficient [16]. Of course, some non-uniformity may also exist upstream of the honeycomb filter.

Finally, it is worth underlining that the non-uniformity of the total pressure across model volume translate into a non-uniformity of dynamic pressure that is less than $\pm 0.3\% \times q_0$, and therefore satisfies flow quality requirements (see Table 1).

Figure 15. Distribution of total pressure across the test section

5.6   Tunnel static pressure calibration

The calibration laws for the static pressure are examined in Figure 16, for two different static reference taps (C18 and C20). The overall trend with Mach number is well reproduced by the simulation, but not the weak trend with Reynolds number. Interestingly, changing the uniformity of total pressure on the inlet has a small but significant effect ($+0.6\% \times q_0$) on the calibration law.

Since the simulations were not intended to replicate possible geometrical flaws around the taps and on the taps themselves, a perfect match was not expected. Hence the virtual tunnel has calibration laws that are comparable in magnitude and trends, but still different, from those of the real tunnel. As a consequence it is recommended never to use experimentally determined calibration laws to run a CFD model of the tunnel. In this example, it would result in errors of up to about 1% in dynamic pressure.

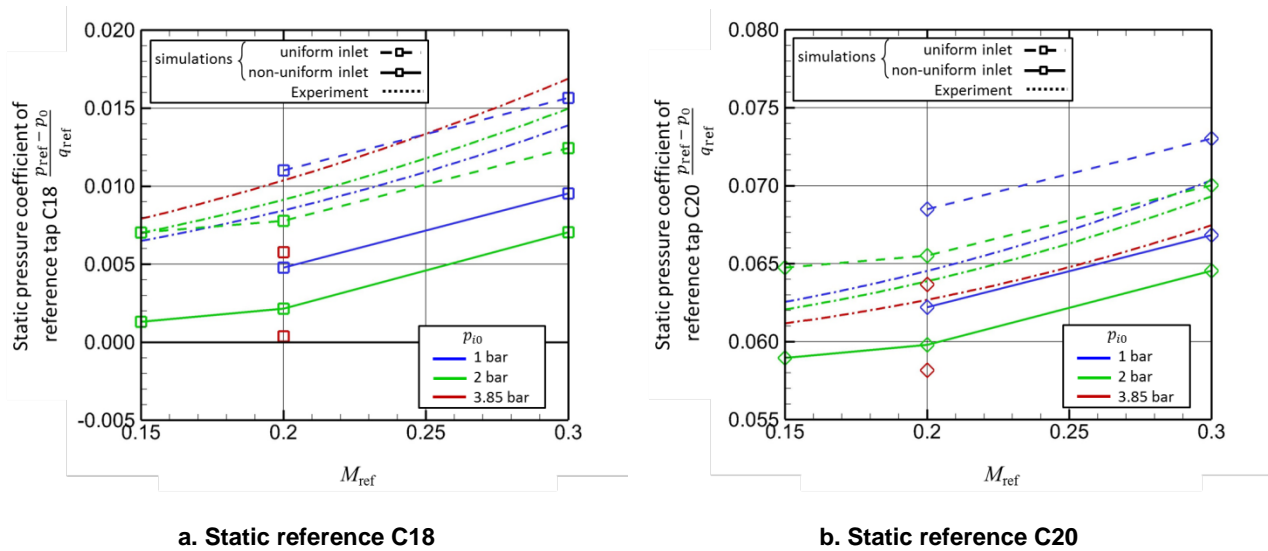a. Static reference C18   b. Static reference C20

Figure 16. Calibration laws for static pressure on two reference taps

6   DISCUSSION ON POSSIBLE SIMULATION IMPROVEMENTS

6.1   Tunnel geometry

Although the tunnel CAD model is not perfect (especially the modelling error causing the "dip" on the starboard side mentioned in section 5.4), 3D scans carried out after the simulations did not reveal large deviations from the theory: deviations were mostly symmetrical, mostly below ±2 mm in the test section, and mostly below ±20 mm in the convergent. It would be worth to attempt integrating these small deviations in the CAD model, but it is not expected that it would improve the simulation significantly.

As already mentioned in section 4, some features of the geometry were neglected on purpose in the simulations, due to their geometrical complexity. It is of course difficult to assess whether or not these features may have an effect on the tunnel flow, however an example of such feature will be given here.

This concerns the venting system at the entrance of the convergent, sketched in Figure 17. Pressure is not exactly uniform along the venting slot. Therefore a weak flow circulation must exist in the back side of the convergent, which redistribute some massflow sidewise. It was expected that this had a very minor effect on boundary layer development at the entrance of the convergent.
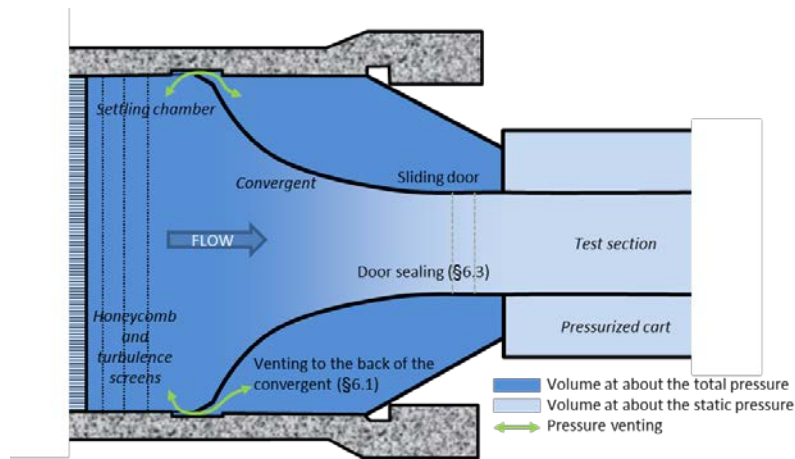
Figure 17. Schematic view of the convergent architecture

Unfortunately, this slot is located in a small area of flow separation identified by the calculation (only at the lowest Reynolds number simulated) and shown in Figure 18. This separation was afterwards confirmed experimentally with tuft visualization, although with a much smaller size. It is created by the locally adverse pressure gradient in front of the steep convergent. Even if the simulations predict that this separation plays no significant role on the mean flow in the test section, one can wonder if the venting slot may play a role on the separation, maybe modifying its extent.

There are chances that many wind tunnels present such small geometrical details that are difficult to model, but may still have an influence on the flow.
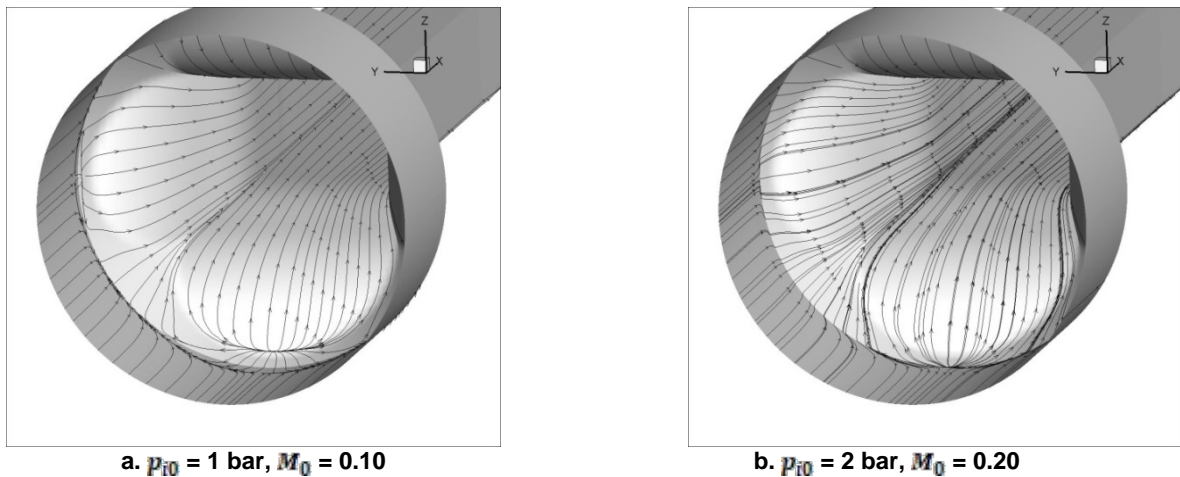

a. p_{i0} = 1 bar, M_0 = 0.10

b. p_{i0} = 2 bar, M_0 = 0.20

Figure 18. Simulated friction lines in the convergent

6.2   Upstream flow

As exemplified in section 5.5, simulations could probably be improved thanks to a better modelling of the flow occurring in the settling chamber, more especially the effect the settling devices (honeycomb and turbulence screens) have on the flow.

In the present work, and even in more recent and more advanced similar simulations (e.g. [19],[22],[23],[24], and [25]), the geometry of the settling devices was completely eliminated from the simulation and their effect was either ignored, or modelled through specification of the inlet boundary condition. This approach requires a "mapping" of the flow in the settling chamber that is detailed enough to come up with a suitable

boundary condition. In the author's opinion, this mapping of the flow can be carried out in the test section, instead of in the settling chamber. Indeed, experimentally characterizing the flow in the test section is not only easier than in the settling chamber, but it is also beneficial to the wind tunnel data quality in general. Simulations can then be used to derive an inlet boundary condition that matches the test section measurements. In the present work, this approach was applied to the case of total pressure with good results (see section 5.5). Because the flow through the convergent is very weakly diffusive, this would probably work for other flow quantities as well.

An opposite strategy would be to completely simulate the geometry of the settling devices. In the F1 wind tunnel, this would mean meshing the honeycomb (about 209 000 cells) and the three turbulence screens (about 13.6 million holes in total). This seems far out of reach for three reasons: the computational power required would obviously be enormous, accurate geometrical input is lacking (such as the orientation of honeycomb cells, the actual distribution of wire diameter on the screens), and physical modelling of such flow would be challenging. Regarding this topic, one has to remember than even tiny geometrical details such as the dirt accumulated on the screens [16], or the way screen pieces are welded together [26] can have an effect on the flow in the test section. Therefore, this strategy of representing only the geometry and let the simulation resolve all the physics in the settling chamber seems unlikely to be successful.

An intermediate way between these two extreme strategies may exist: for instance, by modelling the settling devices as surface flow discontinuities with physical models for the jump in momentum. These physical models would probably present some empirical coefficients that could be set based on available knowledge and measurements. At least the resistance and refraction coefficients [2] would need to be supplied, and they could possibly be non-uniform across the discontinuity surface, and depending on the Reynolds number. Some model to predict the shape of the screen under wind loads could also be incorporated. One can therefore realize that more or less sophisticated models can be built, and they can be adapted to the level of detail experimentally available, and physically required, to model the flow.

6.3   Unknown tunnel features

This last section is about a simple fact: undocumented features of the wind tunnel cannot be reproduced in a simulation model, and their effect on the flow will be missed.

For instance, considering the convergent architecture (already sketched in Figure 17), the back side of the convergent is pressurized at the total pressure of the tunnel, whereas the tunnel flow is near the tunnel static pressure at the end of the convergent. In this area, the tunnel is crossed by the sliding door used when depressurizing the test section. This door is fitted with inflatable sealing to prevent leakage. In case the sealing fails to work properly, flow would leak from the back side of the convergent towards the entrance of the test section. In the early years of F1, several mechanisms were put in place to make sure such a leakage never goes undetected, since it can have an effect on the tunnel calibration.

From a simulation standpoint, one has to be aware that such a leakage can exist, in order to stand a chance to include its effect in the simulation. Even then, its exact properties would be very difficult to document and to translate into a CAD model or boundary conditions (e.g. the location and shape of the leak path, or the mass flow). If tunnel simulations were carried out to troubleshoot such unsatisfactory tunnel behaviour, the result would be disappointing because simulations on their own often cannot spot the source of the issue.

7   CONCLUSION

At first sight, the simulations approximately reproduced the flow field in the simulated part of the F1 wind-tunnel, by properly reproducing the rather simple flow physics involved. Nevertheless, when looking at the result with a more demanding level of detail, as required for the application (see Table 1), they failed to predict some significant features as summarized in Table 2. Possible reasons for this were discussed in section 6 with the help of some examples.

Generalizing these findings to other tunnels is of course difficult, but may be attempted as follows:

- It is feasible to drive the virtual tunnel to a given Mach number thanks to an iterative process on the tunnel back pressure, with a moderate overhead in computational effort. Experimental measurement of this back pressure level is not necessary and textbook methods can provide an appropriate starting point.

- Even in simple wind-tunnels, there may exist geometrical details that are often not represented on drawings or CAD models. As built geometry should be used whenever possible. A visual inspection of the tunnel is also useful in determining what to incorporate in the numerical model.

- Although it drives a lot of what happens in the test section, it seems presently impossible to completely simulate the flow in the settling chamber. Some modelling of the settling devices is necessary and requires both physical modelling and experimental inputs. For that purpose, measurements are not necessarily carried out in the settling chamber itself, but rather in the empty test section.

- Using simulations to troubleshoot non-understood tunnel behaviour may be disappointing since the cause of the issue often cannot be spotted, unless explicitly introduced in the CAD model or boundary conditions.

- Calibration of the wind tunnel should be understood before running the simulations. Using the calibration laws of the physical tunnel to run the virtual tunnel should be avoided. It is preferable to establish calibration laws for the virtual tunnel.

In conclusion, CFD is indeed a very powerful tool that can be used with beneficial outcome, as was already observed in previous publications, e.g. [9][23][25][27]. Nevertheless, as in many other scientific fields, numerical simulation is only a tool and it does not replace physical understanding, academic knowledge, practical sense, engineering judgment or professional experience. In that respect, it is never a waste of time to go through classical textbooks such as [16], [28], [29], or even [30] before pouncing on a computer to run simulations.

Table 2. Summary of expected and achieved results

Topic	Expected / Required	Obtained	Conclusion
Convergence of simulations	Convergence towards steady state at target Mach number	Achieved within reasonable computational effort with the help of a simple control algorithm.	The virtual tunnel can be driven by iterating on the back-pressure, to converge some point of the flow towards a given Mach number and the simulation to steady state.
Overall flow physics	Predict pressure recovery in the diffuser, and boundary layer thickness	Good result.	Overall, RANS modelling is well adapted to the flow physics simulated.
Tunnel calibration	Reproduce tunnel calibration laws for static and total pressure	Orders of magnitude and trend with Mach number are properly retrieved. Trend with Reynolds number is not.	Avoid using experimental calibration laws to run a virtual tunnel.

Topic	Expected / Required	Obtained	Conclusion
Flow uniformity in model volume	Reproduce small non-uniformities in the flow field	A very uniform flow field was obtained, unless when non-uniformity was introduced "by hand" on the inlet (total pressure).	Small non-uniformities originate from features that were not simulated (e.g. settling devices).
Flow unsteadiness, turbulent content	Reproduce turbulent fluctuations of velocity and pressure	Of course, RANS model can give no indication on flow unsteadiness in the free-flow turbulence of the tunnel.	Modelling is not adapted. Besides, sources of turbulence are known to be spread around the whole tunnel circuit.
Guidelines for improvement of the tunnel	Locate tunnel features that can be improved and quantify expected improvements	Small flow separation identified upstream of the convergent (only at low Reynolds number). Clues about non-uniformity in total pressure. No indication for flow angle.	CFD is helpful in some instances, but must be completed with other analyses.

8   ACKNOWLEDGMENTS

REFERENCES

[1] Tinoco, E.N. *et al.*, "Summary Data from the Sixth AIAA CFD Drag Prediction Workshop: CRM Cases", *Journal of Aircraft*, Vol. 55, No. 4, 2018.

[2] Batchelor, G.K., *The Theory of Homogeneous Turbulence*, Cambridge University Press, 1967.

[3] Taylor, N.J. and Rumsey, C.L., "CFD Validation Experiments: Toward a Broader Perspective", paper AIAA 2021-1933, *AIAA Scitech 2021 Forum*, virtual event, 11–15 & 19–21 January 2021.

[4] Krynytzky, A. J., Fleming, M., Sommerfield, D. M., and Li, P., "Computational Modeling of a Slotted Wall Test Section", AIAA Paper 2012-2863, *28th Aerodynamic Measurement Technology, Ground Testing, and Flight Testing Conference*, New Orleans, Louisiana, USA, 25-28 June 2012.

[5] Nayani, S., Sellers, W., Tinetti, A., Brynildsen, S., and Walker, E., "Numerical Simulation of a Complete Low-Speed Wind Tunnel Circuit," AIAA Paper 2016–2117, *54th AIAA Aerospace Sciences Meeting*, San Diego, California, USA, 4-8 January 2016.

[6] Ewald, B.F.R (Ed.), *Wind Tunnel Wall Corrections*, AGARD AG-336, 1998.

[7] Bosnyakov, S et al., Computational tools for supporting the testing of civil aircraft configurations in wind tunnels, *Progress in Aerospace Sciences*, Vol. 44, 2008, pp 67-120.

[8] Hashimoto, A., and Kohzai, M., "Wall Interference Analysis by Whole Wind Tunnel CFD", *5th Symposium on Integrating CFD and Experiments in Aerodynamics*, Tokyo, Japan, 3-5 October 2012.

[9] Hantrais-Gervois, J.L., Cartiéri, A., Mouton, S. and Piat, J.F., "Empty Wind Tunnel Flow Field Computations", *International Journal of Engineering Systems Modelling and Simulation*, 2010, Vol.2 No.1/2, pp.46 – 57.

[10] Mouton, S., "Numerical Investigations of Model Support Interference in Subsonic and Transonic Wind Tunnel", *8th ONERA-DLR Aerospace Symposium*, Göttingen, Germany, October 17-19, 2007.

[11] Pierre, M., « Soufflerie subsonique pressurisée F1 du centre du Fauga-Mauzac de l'ONERA » ("Subsonic Pressurized Wind-Tunnel F1 on the ONERA Fauga-Mauzac Test Center"), paper ICAS B 3-04, *11th Congress of the International Council of the Aeronautical Sciences*, Lisboa, Portugal, September 11-16, 1978.

[12] Carrara, J.-M., and Masson, A., "Three Years of Operation of the ONERA Pressurized Subsonic Wind Tunnel", paper ICAS-80-23.1, *12th Congress of the International Council of the Aeronautical Sciences*, Munich, Germany, October 12-17, 1980.

[13] *Calibration of Subsonic and Transonic Wind Tunnels*, AIAA Recommended Practice R-093-2003, 2003.

[14] Masson, A., *Synthèse des mesures enregistrées entre 1976 et 1986 sur le fonctionnement aérodynamique de la soufflerie F1* (Synthesis of measurements collected between 1976 and 1986 on the aerodynamics of F1 wind tunnel), Onera technical report N°023/3236 GN, June 1987.

[15] Woodward, D.S., François, G., Taylor, N.J., "The Aerodynamic and Structural Design of the DRA 5-Metre and ONERA F1 Low-Speed Pressurised Wind Tunnels", *Aerodynamics of Wind Tunnel Circuits and their Components*, AGARD-CP-585, 1997.

[16] Barlow, J.B., Rae, W.H. Jr., and Pope, A., *Low-Speed Wind Tunnel Testing*, 3rd edition, John Wiley & Sons, 1999.

[17] Masseboeuf, S., Mouton, S., Mariani, R., and Leclaire, B., "Clinometric Measurements by Means of High-Accuracy PIV in the ONERA F1 Low-Speed Pressurized Wind-Tunnel", *13th Asian Symposium*

on Flow Visualization, Novossibirsk, Russia, June 22-26, 2015.

[18] Steinle, F., and Stanewsky, E., *Wind Tunnel Flow Quality and Data Accuracy Requirements*, AGARD Advisory Report No. 184, 1982

[19] Lee, H.C., Pulliam, T.H., Rumsey, C.L., Neuhart, D.H., and Kegerise, M.A., "Simulations of the NASA Langley 14×22 Subsonic Wind Tunnel for the Juncture Flow Experiment", *Advanced Wind Tunnel Boundary Simulation*, NATO/STO Meeting Proceedings MP-AVT-284, 2018.

[20] Cambier, L., and Veuillot, J.-P., "Status of the elsA CFD software for flow simulation and multidisciplinary applications", paper AIAA-2008-0664, *46th AIAA Aerospace Sciences Meeting and Exhibit*, Reno, USA, January 7-10, 2008.

[21] Nayani, S., Sellers, W., Brynildsen, S., and Everhart, J., "Numerical Study of the High-Speed Leg of a Wind Tunnel," AIAA Paper 2015–2022, *53rd AIAA Aerospace Sciences Meeting*, Kissimmee, Florida, USA, 5-9 January 2015.

[22] Rivers, M.B., Nayani, S.N., Tinetti, A., Brynildsen, S.E., and Ferris, R.J., "Numerical Study of the High-Speed Leg of the National Transonic Facility", *Advanced Wind Tunnel Boundary Simulation*, NATO/STO Meeting Proceedings MP-AVT-284, 2018.

[23] König, B., Fares, E., and Wright, M.C.N., Lattice-Boltzmann Simulation of the ETW Slotted Wall Test Section, *Advanced Wind Tunnel Boundary Simulation*, NATO/STO Meeting Proceedings MP-AVT-284, 2018.

[24] Chwalowski, P., Silva, W.A., Wieseman, C.D, and Heeg, J., "CFD Model of the Transonic Dynamics Tunnel with Applications", *Advanced Wind Tunnel Boundary Simulation*, NATO/STO Meeting Proceedings MP-AVT-284, 2018.

[25] Hantrais-Gervois, J.-L., and Piat, J.-F., "A Methodology to Derive Wind Tunnel Wall Corrections with RANS Simulations", *Advanced Wind Tunnel Boundary Simulation*, NATO/STO Meeting Proceedings MP-AVT-284, 2018.

[26] Michel, U., and Froebel, E. "Flow Unsteadiness in Three Low-Speed Wind Tunnels", *Aerodynamic Data Accuracy and Quality: Requirements and Capabilities in Wind Tunnel Testing*, AGARD Conference Proceedings 429, 1988.

[27] Hantrais-Gervois, J.L., Mouton, S., and Piat, J.F., "RANS Simulations to Compute Wind Tunnel Wall Corrections", *47th AAAF International Symposium of Applied Aerodynamics*, Paris, France, March 26-28, 2012.

[28] Mehta, R.D., and Bradshaw, P., "Design rules for small low speed wind tunnels", *The Aeronautical Journal*, Vol. 83, No. 827, 1979, pp. 443 – 453.

[29] Rebuffet, P., *Aérodynamique expérimentale*, 2ème édition, Librairie Polytechnique Ch. Béranger, Paris, 1958.

[30] Prandtl, L., *Attaining a Steady Air Stream in Wind Tunnels*, NACA Technical Memorandum No. 726, October 1933.

[31] Perin, R., Bècle, J.P., and Desplas, P., "Progress on engine airframe integration aerospatiale's experience in ONERA's large wind tunnels", paper AIAA-94-2559, *25th AIAA Plasmadynamics and Lasers Conference*, Colorado Springs, USA. June 20-23, 1994.

[32] Desplas, P., "35-year structural monitoring of a prestressed-concrete pressurized wind tunnel", *Proceedings of the 6th European Workshop - Structural Health Monitoring 2012*, EWSHM 2012, Vol. 2, 2012, pp. 1109-1115.